coatings

MDPI

Article

Non-Fluorinated, Sustainable, and Durable Superhydrophobic Microarrayed Surface for Water-Harvesting

Oriol Rius-Ayra *, Sheila Fiestas-Paradela and Nuria Llorca-Isern

CPCM Departament de Ciència dels Materials i Química Física, Facultat de Química, Universitat de Barcelona, Martí i Franquès 1, 08028 Barcelona, Spain; shfiestp7@alumnes.ub.edu (S.F.-P.); nullorca@ub.edu (N.L.-I.)

* Correspondence: oriolriusayra@ub.edu

Received: 2 March 2020; Accepted: 24 March 2020; Published: 26 March 2020

Abstract: Water scarcity is a worldwide issue that significantly affects the environment, population, and economy of the arid zones. In this study, we report a straightforward method for water-harvesting based on modifications of the surface wettability. Using magnesium chloride, lauric acid, and electrodeposition process, a superhydrophobic surface (155°) is obtained. Morphological characterization techniques allow determination of the characteristic flower-like microstructures combined with close packed nanoarrays that lead to the hierarchical structure. Furthermore, the coating presents vertically aligned microarrays in a non-linear cone morphology formed by dynamic templating of hydrogen bubbles. From a chemical point of view, magnesium laurate is responsible for the surface tension decrease. To determine the durability of the obtained surface ultra-violet (UV) light test and abrasive paper test, tests are carried out revealing high durability against these severe conditions. The water-harvesting ability of the superhydrophobic surface is studied at 45° and 90° tilted samples. The capacity of the water to be harvested efficiently is found to be at 90° tilt under fog conditions. The use of green reactants associated with this hierarchical structure broadens a new scope for sustainable freshwater collection and it becomes an excellent example of a green solution.

Keywords: non-fluorinated; superhydrophobic; water-harvesting; fatty acid; robust; durable

1. Introduction

Water shortages and scarcity is a worldwide phenomenon that significantly alters the environment as well as the population in arid zones. Moreover, access to safe drinking water remains a challenge in several countries, which leads to the development of new strategies to achieve a new scenario in which materials used must be remarkably sustainable.

Indeed, surfaces with extraordinary wettable properties are attracting attention due to the capability of collecting water from the environment. In fact, surfaces with a water contact angle (WCA) higher than 150° as well as a contact angle hysteresis (CAH) ≤ 10° are defined as superhydrophobic [1,2]. Because of their extraordinary surface properties, novel applications are emerging to solve environmental problems such as oil/water separation in oil spills [3–7], corrosion resistance in marine conditions [8,9], or reducing ice adhesion in cold environments [10,11]. Moreover, water-harvesting in some environments can contribute to solving global issues. Because of that, several complex methods are carried out to collect water droplets by combining superhydrophobic–hydrophilic surfaces such as polymerization [12], templating [13], biotemplating [14] or nanoimprint lithography [15]. Despite the results showing these references, the reactants used to decrease surface tension such as trimethylchlorosilane (TMCS) or perfluorooctyltriethoxysilane (FAS) are combined with solvents such as chlorobenzene or chloroform that are extremely harmful for the environment and human health. Therefore, the development of

innovative and sustainable strategies [16–18] appears to be necessary to generate a new framework for superhydrophobic surfaces. Environmentally friendly materials [19–22] are a forward-looking approach towards materials science because they also play an important role in applications to distinct ecosystems due to their benign properties. For that reason, eco-friendly surfaces without the presence of fluorine compounds remain a challenge [23,24]. Indeed, long-chain fatty acids [25,26] play a key role in this subject because of their intrinsically hydrophobic character. In this direction, different strategies can be found in the literature such as liquid phase deposition (LPD) of cinnamic acid from cinnamon or myristic acid from nutmeg to prepare superhydrophobic copper surfaces [27]. Others rely on the co-precipitation method used to obtain Fe_3O_4 magnetic nanoparticles (MNPs) via an eco-friendly route [28]. Moreover, superhydrophobic polydimethylsiloxane (PDMS) monolith has also been prepared by emulsion templating process [29], or biomass-derived banana peel aerogel from the combination of different techniques allowing separation of oil-in-water systems [30].

In the present research, a new sustainable surface is obtained by electrodeposition of lauric acid with magnesium chloride that leads to magnesium laurate as a main chemical compound responsible for surface tension decrease. This effect combined with the flower-like structures conduced superhydrophobic properties observed (WCA = 155°). To sum up, the as-prepared surface is highly durable and is still superhydrophobic after several cycles against UV light exposure or abrasive test. Finally, the completely superhydrophobic surface is composed of several microarrays in a non-linear cone shape caused by dynamic templating during electrodeposition, which allows water condensation under fog conditions and collects water droplets for human consumption.

2. Materials and Methods

2.1. Electrodeposition

The present methodology is based on electrochemical deposition (EDP) that has been carried out on aluminum substrate UNS A91070 thin plate (10 × 40 × 1 mm) (Servei Estació, Barcelona, Spain) previously grinded with P1200 SiC abrasive paper to clean and remove impurities from the substrate surface. The electrolytic bath is prepared as follows: the reactants, 0.1 M lauric acid (Scharlab, S.L., Barcelona, Spain) and 0.05 M $MgCl_2$ (Panreac, Barcelona, Spain), are dissolved in a solution of absolute ethanol (Scharlab, S.L., Barcelona, Spain). Two aluminum substrates (acting as electrodes) are immersed vertically in the previous solution, which works as the electrolytic bath, and both plates are separated 20 mm from each other. After applying a current density of 0.02 A/dm^2 for 900 s, the superhydrophobic system is deposited onto the cathode. After the electrodeposition, the samples are removed, cleaned with ethanol, and dried in a fume hood for a few seconds.

2.2. Durability Tests

Two different tests are carried out to determine the durability of the as-prepared superhydrophobic surface. On the one hand, the surface is exposed under UV light (λ = 250 nm) using a Philips TUV 8W G8T5 UV lamp with a 25 cm distance between the lamp and the sample. The test allows evaluation of the stability of the surface after 300 min of exposure. On the other hand, a sandpaper abrasive test is also used to determine the surface durability in severe abrasive conditions. The superhydrophobic surface is placed in contact with SiC P1200 sandpaper and it is moved 10 cm across for 10 cycles while a pressure of 5 kN/m^2 is applied. After each abrasion cycle, the WCA as well as the sliding angle (SA) are measured.

2.3. Water-Harvesting Test

To study the water-harvesting ability of the as-prepared sustainable surface, a conventional controlled salt fog chamber (ISO 9227) was set up at room temperature (25 ± 1.1 °C) and a working pressure of deionized water of 172 kPa. All the samples had an area of 10 × 4 mm and were exposed

for 2 h under fog conditions; the weight of the collected water was measured. In addition, the samples were held at two different tilt angles (45° and 90°) to determine any effect in water-harvesting rate.

2.4. Characterization Techniques

Different characterization techniques were used to determine morphological structure as well as the chemical composition of the obtained surface. The sample surface was characterized using FE-SEM JEOL J-7100 electron microscope (JEOL Ltd., Tokio, Japan) in order to study its detailed morphology and energy dispersive X-ray spectroscopy detector (EDS) (Oxford Instruments, Oxfordshire, England) to determine the elemental composition of the surface. Atomic Force Microscopy (AFM) was used to analyze the topographic structure using AFM Multimode 8 Microscope with electronic Nanoscope V (Bruker, Billerica, MA, USA) in Peak Force tapping Mode with a tip Sharp Nitride Lever (SNL) from (Bruker, Billerica, MA, USA) and the cantilever with resonance frequency of 65 kHz and a spring constant of 0.35 N/m. The study of the surface nanostructure was performed with a transmission electron microscope, JEOL JEM-2100 (TEM) (JEOL Ltd. Tokio, Japan) with EDS detector for microanalysis; the samples were supported onto a holey carbon film on a Cu grid. The roughness of the surface was measured by confocal microscopy using a LeicaScan DCM3D on a surface of 1270×950 μm^2 using a white light beam. X-Ray Photoelectron Spectroscopy (XPS) (PHI, Chanhassen, MN, USA) was carried out to determine chemical composition by PHI ESCA-5500 using a monochromatic X-Ray source (Kα (Al) = 1486.6 eV and 350 W); Multipak software was used to perform deconvolutions and calculate the atomic percentage of each element. Attenuated Total Reflectance Fourier Transformed Infrared (ATR-FTIR) spectroscopy was also used to establish the presence of hydrocarbon acid and its chemical bonds; for this purpose, a Fourier Bomem ABB FTLA in the range 4000–525 cm^{-1} at a resolution of 4 cm^{-1} was used. μ-Raman spectroscopy analysis was carried out to determine chemical composition of the obtained surface using a Jobin–Yvon LabRam HR 800 dispersive spectrometer, coupled to an optical microscope Olympus BXFM (Horiba, Kioto, Japan). The CCD detector was cooled at –70°C. Laser lines were 532 nm in a spectral range of 4000–100 cm^{-1}, dispersive gratings at 600 l/mm and at 5 mW power. Phase characterization of the surface was obtained by X-Ray Diffraction (XRD) from PANalytical X'Pert PRO MPD Alpha1 powder diffractometer in Bragg-Brentano θ/2θ geometry of radius 240 millimeters and Cu Kα1 radiation (λ = 1.5406 Å). Contact angle was measured using a digital microscope Levenhuk and 3.5 μL of deionized water at room temperature. The reported WCA values are the average of three measurements of droplets at different parts on the surface. SA were measured when the samples were tilted until water droplets rolled off and CAH were measured by increasing and decreasing droplet volume.

3. Results and Discussion

3.1. Structural Characterization

Field-Emission Scanning Electron Microscopy (FE-SEM) observations were performed to study the surface morphology. After 900 s of EDP, the aluminum substrate surface was completely covered with micro- and nano-structures. The combination of both features causes a hierarchical structure adopting a flower-like morphology that plays a key role in the modification of the surface wettability. These characteristic structures are built up in two distinct levels: the microstructure shown in Figure 1a, formed itself by the nanolayers as seen in Figure 1b.

EDS microanalyses (Figure 1c) of the nanostructure indicated the presence of a carbon peak corresponding to lauric acid and a contribution from the previous carbon sputtering (Kα = 0.277 keV); also, there was a less intensive peak of magnesium appeared in the spectra belonging to the obtained surface layer (Kα = 1.253 keV). Oxygen (Kα = 0.525 keV) and aluminum (Kα = 1.486 eV) are also present in the EDS spectra, both from the substrate as well as the inherent alumina to the aluminum substrate surface. A certain contribution of the substrate and lauric acid ($C_{12}H_{24}O_2$) are confirmed.

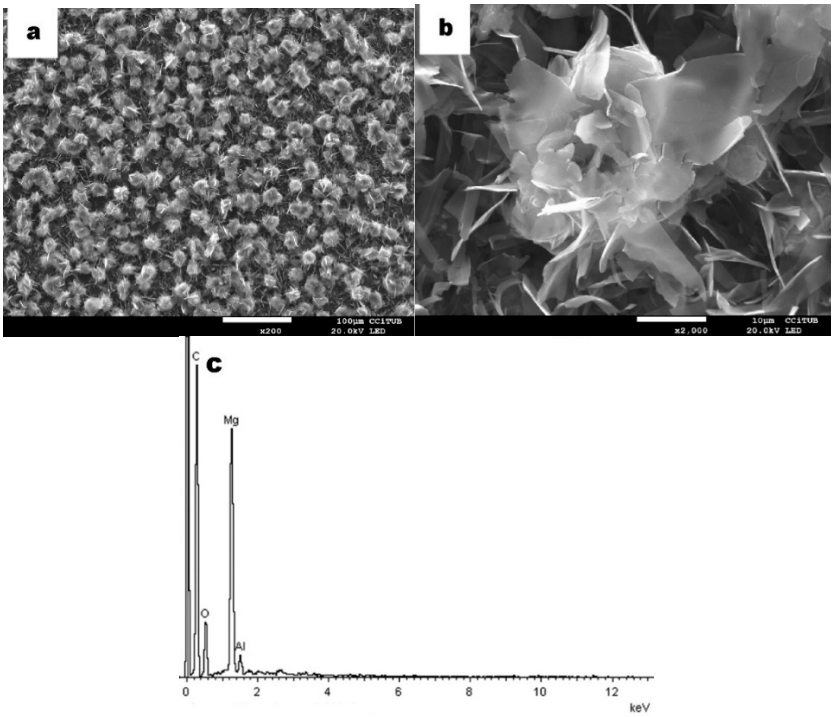

Figure 1. FE-SEM images of the as-prepared superhydrophobic (SH) surface on aluminum substrate: (**a**) distribution of microstructures on the substrate after 900 s of electrodeposition; (**b**) at higher magnification the flower-like structure and its nanostructured layers are observable; and (**c**) EDS microanalysis where Mg and C from the obtained coating and Al from substrate can be identified.

AFM is used as a high-performance imaging technique allowing more accurate analysis of the hierarchical structure of the surface at the nanometer scale. From the AFM observation, the surface of nanolayers is found to be highly organized by lamellar nano-structures in which the smooth layers overlap (Figure 2a,b bottom left) and are highly stacked to each other as can be seen in Figure 2c,d. The layer thickness was measured and was 32.8 ± 2.9 nm.

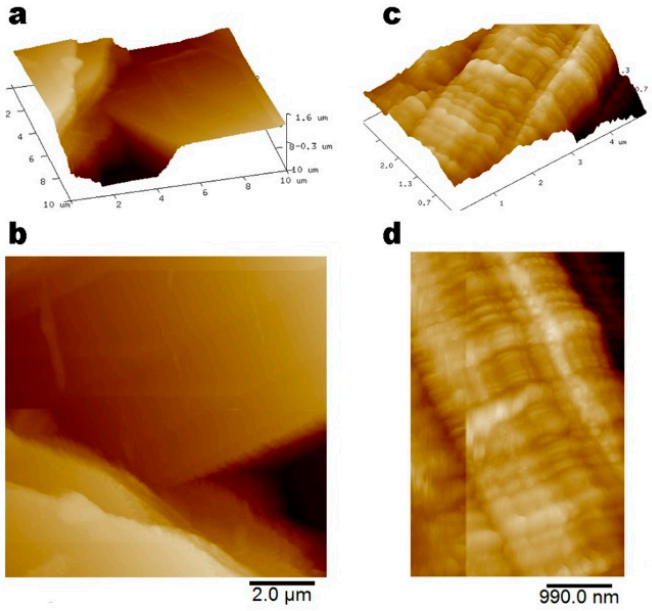

Figure 2. AFM images showing lamellar nano-structures stacked on each other in two different areas: 10 × 10 µm (**a**) (**b**) and 4.0 × 3.4 µm (**c**) (**d**).

High-resolution transmission electron microscopy (HR-TEM) allows observation of the structure at the nanometer scale as well as determination of the elemental composition by EDS microanalysis of the as-prepared SH coating. The structure observed corresponds to the unit (petal) of the flower-like morphology made of thin layers that overlap themselves (Figure 3a) and planes in the layer itself (Figure 3b). These units of the coating do not contain long-range order in the atomic lattice, giving diffuse ring diffraction patterns in the corresponding selected-area electron diffraction (SAED) obtained. The weak diffraction rings in Figure 3c suggest certain arrangements that can be considered crystalline in nature of the petal morphology, consistent with a distinguishable diffraction ring that corresponds to a monoclinic crystal structure according to the Joint Committee on the Powder Diffraction Standards (JCPDS) with data card 8-528. Figure 3d shows the EDS microanalysis in which the magnesium associated with the SH coating is identified (Kα = 1.253 keV). A peak of aluminum from the substrate (Kα = 1.486 keV) and an intense peak of carbon (Kα = 0.277 keV) from the lauric acid and also from the carbon film of the copper grid (Lα = 0.930 keV and Kα = 0.930 keV), chloride peaks (Kα = 2.621 keV) are assigned to the presence of magnesium chloride from the reactant used.

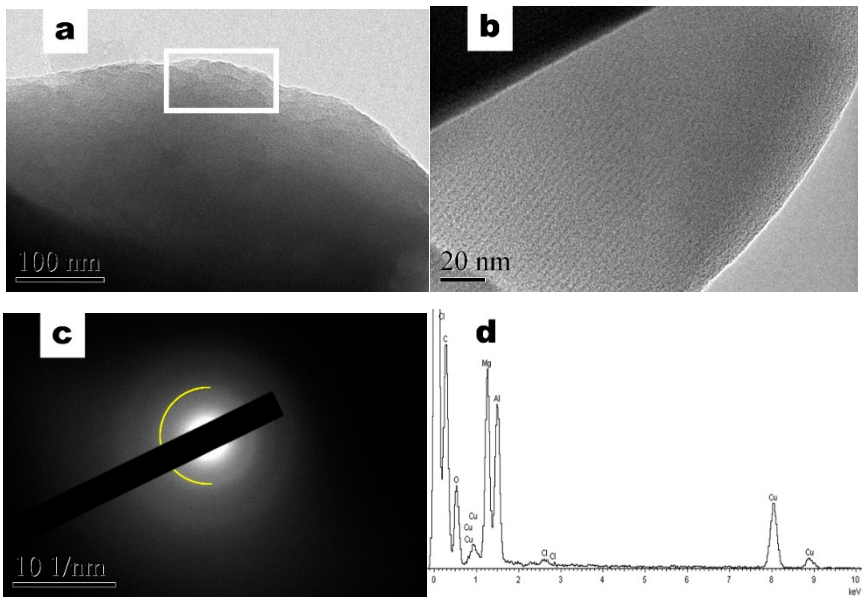

Figure 3. HR-TEM images of the as-prepared coating that is structured in nanolayers that overlap themselves (**a**), (**b**); (**c**) the SAED pattern showing weak rings from nanolayers; and (**d**) the EDS spectrum shows that the composition is mainly Mg and C (as the TEM grid is Cu and Cl are associated with the $MgCl_2$ reactant used).

XRD technique should allow determination of the crystalline character of the surface. As shown in Figure 4, the coating presents five peaks assigned to the aluminum substrate and corresponds to the planes 2θ = 38.5° (111), 2θ = 44.7° (200), 2θ = 65.1° (220), 2θ = 78.2° (311), and finally 2θ = 82. 4° (222). Additionally, a reflection at 2θ = 20.798° is distinguishable (Figure 4 inset) that is characteristic of the lamellar structures of organic compounds arranged in a monoclinic set system that can be assigned to the space group $P2_1/a$ [31–34]. Hence the superhydrophobic surface is made of well-organized layers.

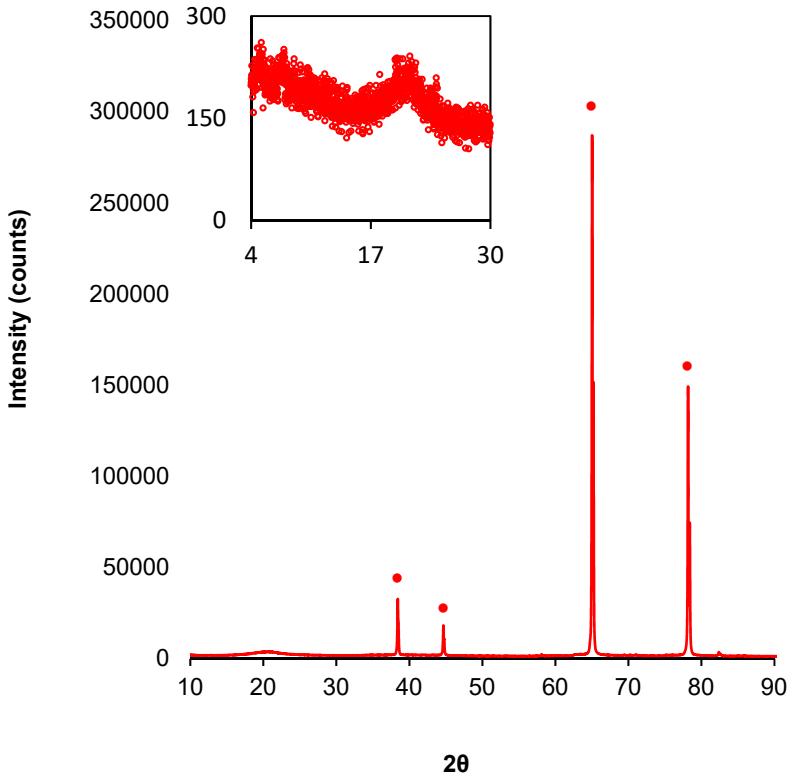

Figure 4. XRD peaks in the inset indicate well-organized layers from an organic lamellar structure at 2θ = 20.798°. Peaks from the aluminum substrate (•) are indicated in the diffractogram.

For structural characterization, let us interpret the surface morphology as the combination of each flower-like feature with nanolayers giving rise to the hierarchical structure. The assembly of these hierarchical structures increases the roughness allowing the air to be trapped in the whole surface pockets producing a Cassie–Baxter wetting regime [35]. In addition, the nanolayers of the superhydrophobic surface are arranged in a monoclinic crystal structure that can be related to greater lateral Van der Waals interactions between laurate chains in the lattice [32].

3.2. Chemical Characterization

Fourier transform infrared spectrometry (ATR-FTIR) is used to determine the chemical composition related to lauric acid as well as to the new eco-friendly coating (Figure 5). Pure lauric acid [36–38] and the formed coating presents different common bands, which are sharp peaks at ca. 2951 cm^{-1}, 2911 cm^{-1} and 2845 cm^{-1} that correspond to stretching of the alkyl chain of $\nu_{as}CH_3$, $\nu_{as}CH_2$, ν_sCH_2-CH_2. At ca. 1470 cm^{-1} weak and broad bands assigned to δCH_2 and δH–C–H bendings can also be found. Finally, both samples coincide in three weak and sharp bands situated at ca. 1122 cm^{-1} that correspond to δCH bending out of plane, ca. 1088 cm^{-1} CH_3 symmetric deformation and ca. 776 cm^{-1} from the vibration of δC-H bending out of plane. For SH coating, the vibration with sharp and very strong band at ca. 1696 cm^{-1} assigned to νC = O stretching is no longer present in the coating [39,40]. Moreover, sharp and medium intense band at ca. 1300 cm^{-1} is assigned to νC–O stretching and two sharp and medium intense bands at ca. 1192 cm^{-1} and ca. 934 cm^{-1} are assigned to the stretching vibration of –OH group. In contrast, superhydrophobic coating presents three distinct sharp and weak bands at ca. 1559 cm^{-1}, ca. 1442 cm^{-1} and ca. 1408 cm^{-1} that are assigned to the vibrations of $\nu_{as}COO^-$, $\nu_{as}COO^-$, and ν_sCOO^- stretching, respectively. This characteristic difference indicates that no free lauric acid on the surface is left after the electrodeposition and a new functional group is formed assigned to carboxylate formation (COO^-).

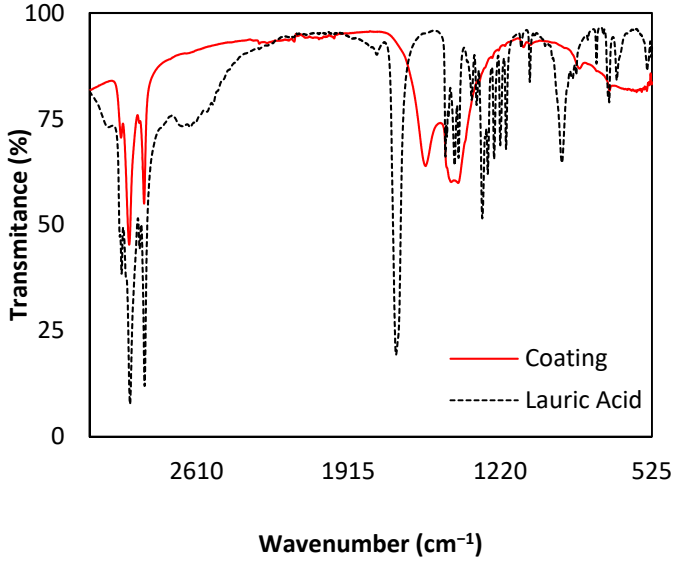

Figure 5. ATR-FTIR spectroscopy technique allows determining the formation of carboxylate compound after the electrodeposition process.

μ-Raman spectroscopy was used to complement ATR-FTIR and determine the chemical composition and consequently the presence of laurate. This characterization technique is particularly important because it reveals the characteristic fingerprint for organic compounds due to alkyl chain [41,42]. Figure 6 depicts the Raman spectrum of the obtained superhydrophobic surface where four types of group bands can be identified. The first region below 1000 cm^{-1} corresponds to low-frequency bands and are assigned to γCH_2 rocking vibration [43,44]. The group of bands between 1064 cm^{-1} and 1123 cm^{-1} are assigned to symmetric $\nu_s C–C$ symmetric stretch [45]. Bands between 1295 cm^{-1} and 1446 cm^{-1} correspond to δCH_2 and δCH_3 bending [44,46]. At 2735 cm^{-1} can be found a band also assigned to δCH_2 bending. Finally, ca. 2900 cm^{-1} this group of strong bands are assigned to $\nu C–H$ stretch [43]. Those bands are characteristic of lauric acid derivative such as magnesium laurate.

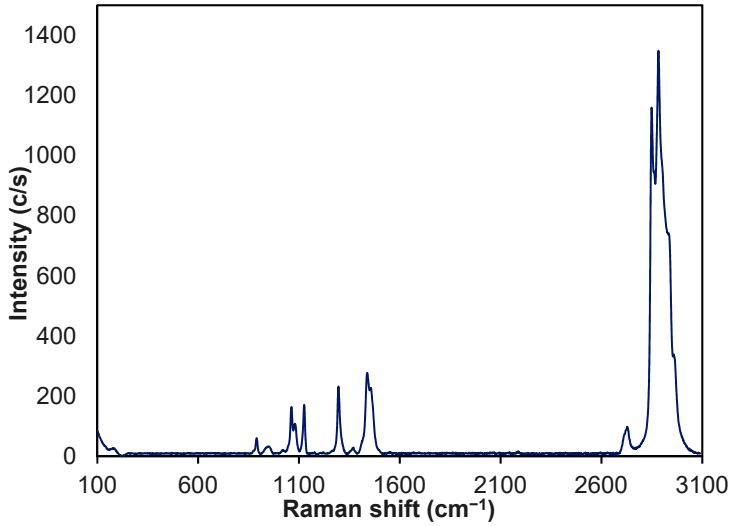

Figure 6. Raman spectrum of superhydrophobic coating assigned to laurate because of the fingerprint of alkyl chain.

Comparing the spectra of Raman with the ATR-FTIR, it can be found that weak bands assigned in ATR-FTIR such as C–H vibrations are strong in Raman spectrum and vice versa, which is a common

behavior between both spectroscopic techniques. This particularity allows determination of the chemical composition of the as-prepared superhydrophobic surface assigned to laurate group.

High-Resolution (HR) XPS was used to investigate the chemical composition as well as the chemical environment of the obtained superhydrophobic coating. The HR-XPS spectra shows C-1s, O-1s, and Mg-2s of the coating after 900 s of EDP and the atomic concentration is 77.65% of C-1s, 18.06% for O-1s, and 1.998% of Mg-2s. It is worth noting the presence of Ca-2s (1.01 %), which is considered an impurity of the reactants. The peak in the C-1s region can be deconvoluted in three distinct components (Figure 7 a) corresponding at 282.7 eV to C-C bond, 285.6 eV to carbonyl group (C = O) form the carboxylate and finally 289.2 to carboxylate group (O–C = O) [47,48]. The O-1s spectra is deconvoluted to three peaks (Figure 7b) assigned to C = O at 530.1 eV, C-O bond at 532.7 eV and O–C = O from the carboxylate group at 535.2 eV bonded to a metallic atom [48,49]. For Mg-2s spectrum the deconvolution (Figure 7 c) presents a peak at 90.57 eV from Mg (II) oxidation state [50].

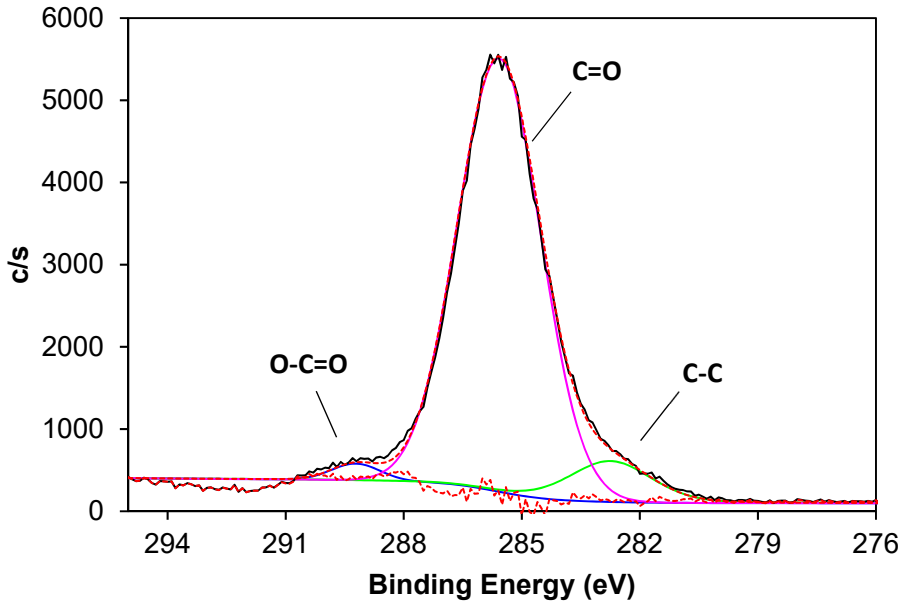

(**a**)

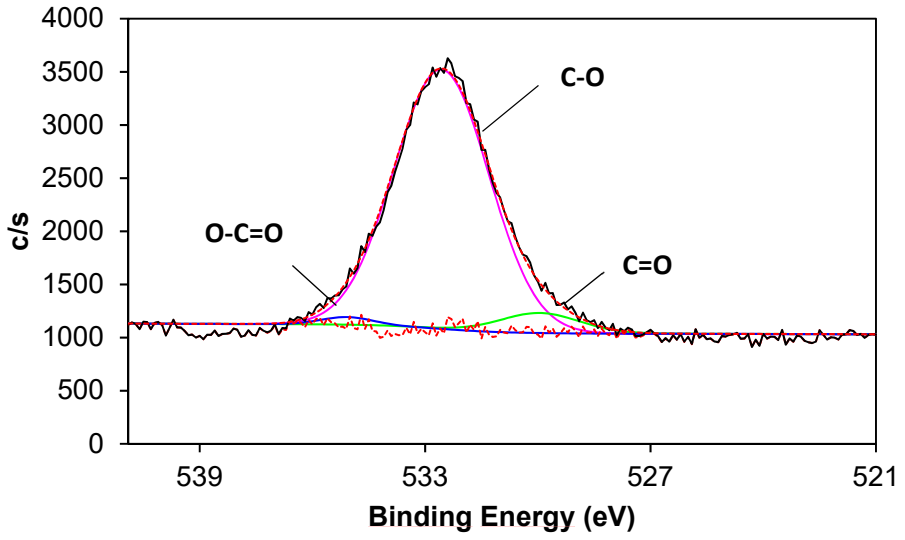

(**b**)

Figure 7. *Cont.*

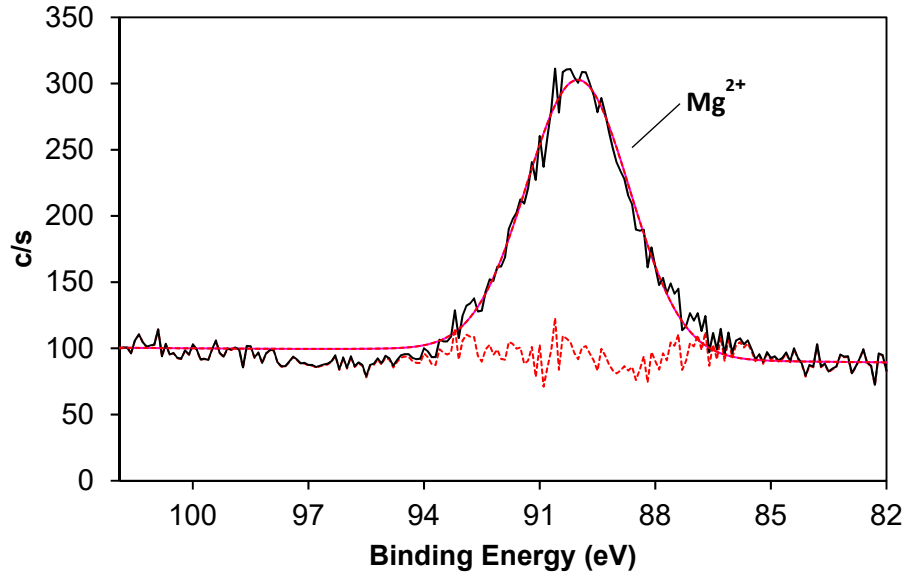

(**c**)

Figure 7. HR-XPS confirms the generation of a magnesium carboxylate after the EDP that decreases the surface tension of the as-prepared coating (**a**) C-1s, (**b**) O-1s and (**c**) Mg-2s.

The combination of these spectroscopic techniques allows the determination of the chemical composition of the as-prepared superhydrophobic surface. Taking into account the ATR-FTIR, it shows the characteristic bands of carboxylate group after EDP of lauric acid combined with $MgCl_2$ while in Raman spectrum the fingerprint of laurate alkyl chain is found. Moreover, O-1s and C-1s HR-XPS spectra reveals the presence of carboxylate functional group bonded to a metallic atom that is assigned to magnesium (II) as depicted in Mg-2s spectrum. Taking into account these results, the main component of the system is assigned to magnesium laurate ($Mg(C_{11}H_{20}COO)_2$) that contributes to decrease the surface tension of the final system.

From an electrochemical point of view, near the aluminum surface, magnesium (II) ions react with lauric acid while it releases H^+ to the hydro-alcoholic medium that tends to increase its concentration locally [51,52].

$$Mg^{2+} + 2C_{11}H_{20}COO^- \rightarrow Mg(C_{11}H_{20}COO)_2$$

Water is oxidized onto the anode while magnesium laurate is formed on to the cathode where at the same time it also takes place hydrogen evolution reaction (HER):

$$H_2O_{\,(l)} \rightarrow O_{2\,(g)} + 4H^+_{(aq)} + 4e^-$$
$$2e^- + 2H^+_{(aq)} \rightarrow H_{2\,(g)}$$

Therefore, meanwhile, magnesium laurate flower-like microstructures are formed through the whole surface of aluminum substrate, and hydrogen bubbles promote the obtained coating, itself vertically aligned in microarrays due to its detachment and vertical flow, which is an indication that hydrogen bubbles perform as a dynamic template. The obtained morphology of microarrays is characterized using confocal microscopy, as shown in Figure 8.

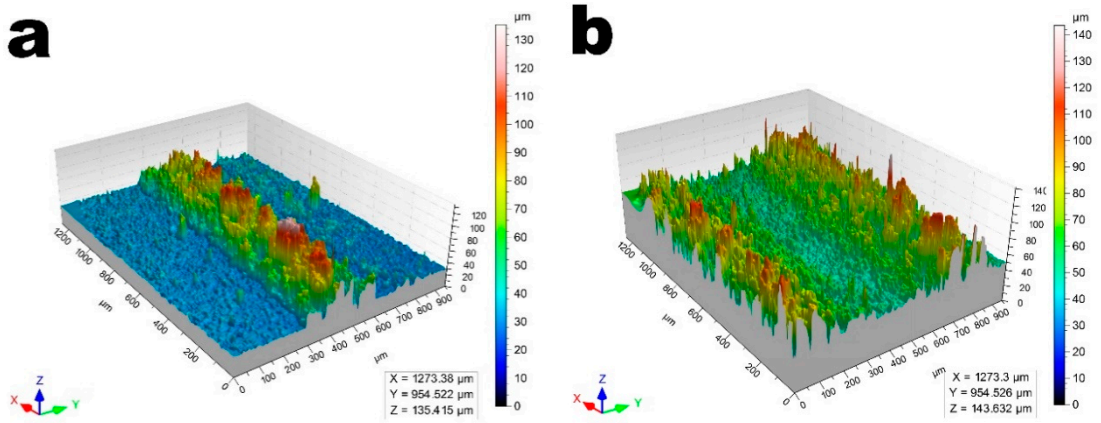

Figure 8. Confocal microscopy images show: (**a**) the formed microarrays in a non-linear cone shape and (**b**) pitch between cones. These features were caused by dynamic templating of hydrogen bubbles during electrodeposition of magnesium laurate.

The morphology of microarrays can be defined as a non-linear cone shape with 20° tip angle, 285.4 ± 22.5 µm base length, and height 21.7 ± 7.3 µm while lower tip angle is 57° (Figure 8a). Additionally, the distance between two consecutive non-linear cones, known as pitch, is 795.9 ± 5.6 µm (Figure 8b).

3.3. Wettability Properties

Superhydrophobicity is precisely defined by several parameters related to the angle between a surface and a water droplet such as WCA, SA, and CAH [2,53]. In our case, after 900 s electrodeposition process the WCA = 155° ± 0.6° and the as-prepared surface shows superhydrophobic properties and the SA is also measured and results 5° ± 0.1° (Figure 9a,b). Furthermore, CAH = 1 ± 0.5°. Considering these results, it can be concluded that water droplet roll-off across the surface.

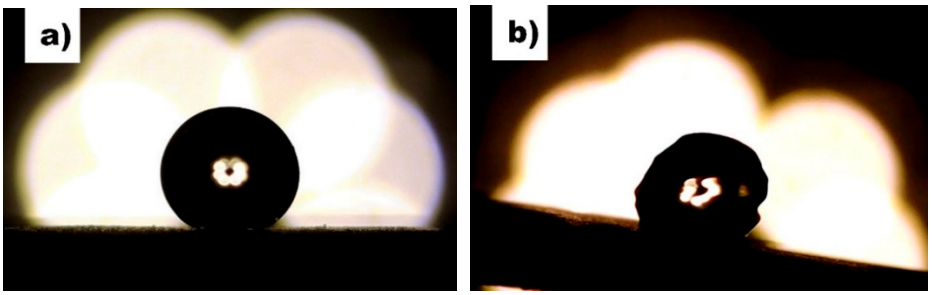

Figure 9. Images of contact angle measurements: (**a**) WCA = 155 ± 0.6° and (**b**) SA = 5 ± 0.1°. Both characteristics leads to a superhydrophobic surface with self-cleaning properties.

Moreover, it is important to study the behavior of these coatings under different conditions to understand and determine their durability. Hence, UV light resistance test [54] is carried out to determine the capability of the superhydrophobic surface to resist environmental conditions. After 300 min of UV light exposure (Figure 10), there was no remarkable difference in the WCA between the coating before the test and after 300 min under UV light exposure. Indeed, the WCA remained higher than 150° after every exposure leading to a durable superhydrophobic surface in these conditions. Regarding the SA, it slightly increased from 5° to 7° and because the value was still lower than 10° after the UV tests, it indicates the robustness of the SH surface under UV light conditions.

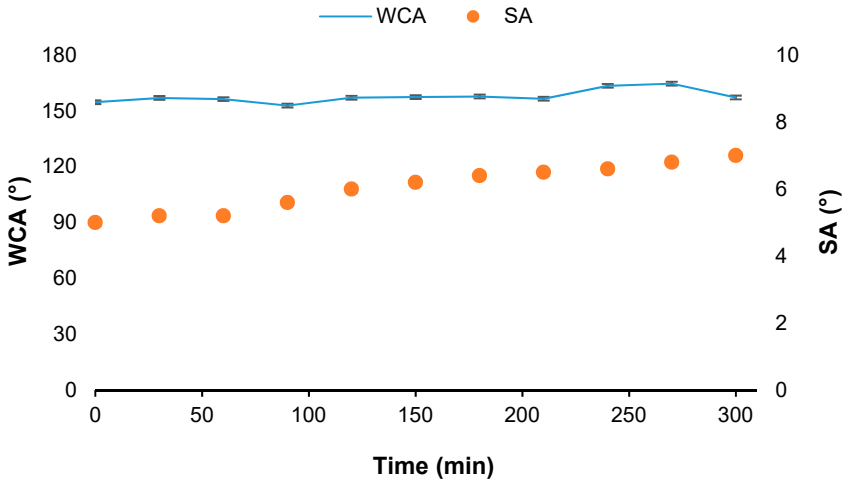

Figure 10. After several cycles of UV light test the WCA is not affected at all, which denotes a high stability of the coating under energetic light. SA increases slightly but it still presents self-cleaning properties after 300 min under UV light exposure.

Taking into consideration the resistance against severe mechanical test, a sandpaper abrasion test (SiC P1200) was performed because it is an effective method to evaluate the durability against mechanical abrasion of superhydrophobic surfaces. The test consists of forcing the contact between the surface and the abrasive paper with an applied pressure of 5 kN/m^2 through 10 cm, this test is repeated 10 times. After the first abrasive cycle, a white powder could be found on the sandpaper although the WCA remains higher than 150° in the coated sample. Despite this residue and after 10 cycles (Figure 11a), the surface is still superhydrophobic and the corresponding WCA was also measured with a value of 152° and SA = 6°. The results indicate high durability of the SH surface and maintains its self-cleaning properties despite the sigmoidal increase after the fifth cycle (Figure 11a) caused by a decrease in roughness. Furthermore, self-cleaning properties of superhydrophobic surface after abrasion test were also investigated. Typically, a layer of soot was poured over the surface, which was tilted 6°, and the water droplet easily slides along the surface while soot powder was pick up and the surface was completely cleaned (Figure 11b). This result reveals that despite mechanical abrasion against the surface, it retains high WCA and low SA where both features are responsible for low adhesion and self-cleaning properties.

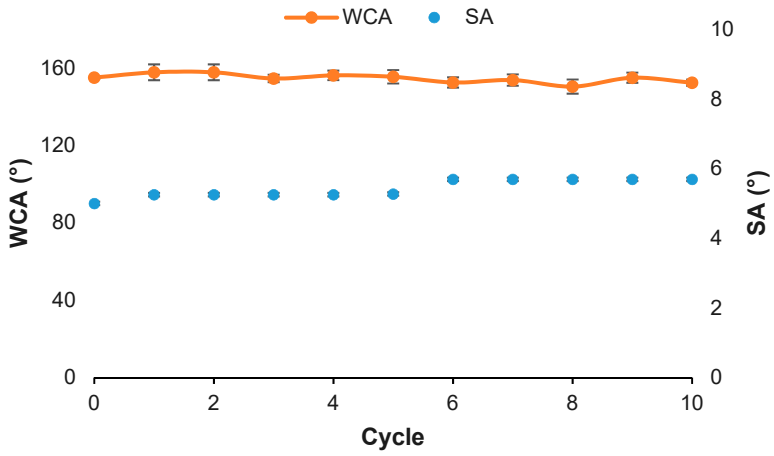

(**a**)

Figure 11. *Cont.*

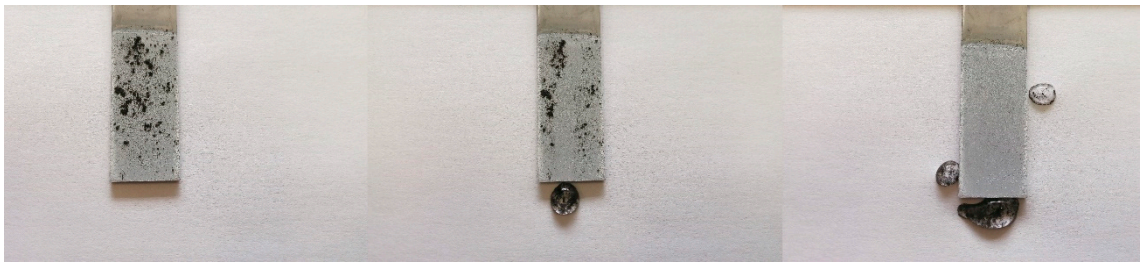

(**b**)

Figure 11. Durability of the as-prepared coating is showed by (**a**) WCA remains slightly constant and higher to 150° after each sandpaper abrasive cycle while SA increases until a maximum value of 6°; and (**b**) self-cleaning properties were investigated after abrasive paper test.

As the roughness of the surface samples plays a key role to define the superhydrophobic character [1], RMS (root-mean-square) is measured using confocal microscopy. Before EDP, aluminum substrate shows RMS = 0.52 ± 0.16 μm (Figure 12a) whereas after that process, the superhydrophobic surface takes a value of 8.59 ± 0.39 μm (Figure 12b). An increase in the roughness of the surface will lead to a rise in the superhydrophobic character of the as-prepared surface. The results of RMS values of the as-prepared coating are compared with the measured RMS after sandpaper abrasion test where RMS takes a value of 2.99 ± 0.76 μm (Figure 12c).

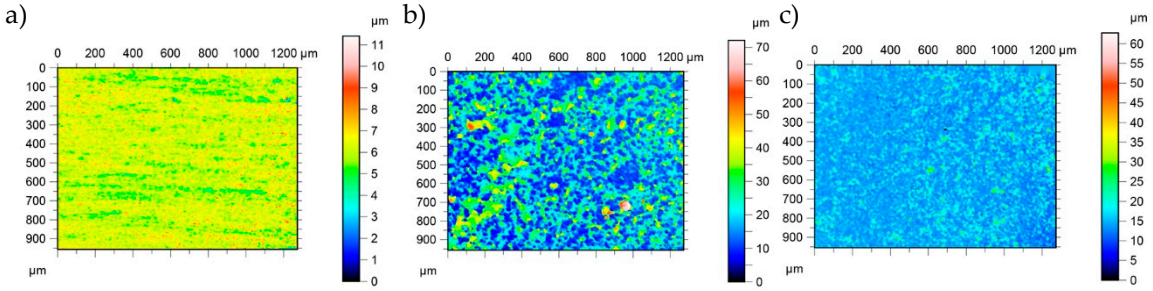

Figure 12. RMS values measured by optical confocal microscopy are aluminum substrate (**a**) 0.52 ± 0.16 μm; superhydrophobic surface (**b**) 8.59 ± 0.39 μm and after 10 cycles of abrasion test (**c**) 2.99 ± 0.76 μm. The EDP process increases the roughness while the abrasion test reduces it.

The difference between the RMS values before and after the sandpaper abrasive test is due to its ability to smooth the surface. Despite decreasing the value of roughness, the superhydrophobic character is not severely affected (WCA = 152°) and it remains superhydrophobic. To better comprehend the resistance against abrasive paper test and evaluate the durability of the as-prepared surface, FE-SEM is used to determine the morphology of the surface after 10 cycles and EDS allows identification of the semiquantitative composition before and after the test. It can be seen that the flower-like structure (Figure 13a) is no longer present at the upper structures and in fact they are smoother compared with the previous morphology (Figure 1). Despite this, several bumpy structures are present and composed of a hierarchical structure. In addition, the elemental composition of the surface after the abrasive paper test is determined and compared using EDS microanalyses (Figure 13b). The spectrum shows that the composition is the same compared to the coating before abrasive test (Figure 1c) but the peak assigned to Mg is less intense than the coating itself before abrasion. These results demonstrate that the composition does not change significantly after the coating surface is damaged by abrasive paper test. This illustrates that the hierarchical structure of the as-prepared coating is chemically homogeneous.

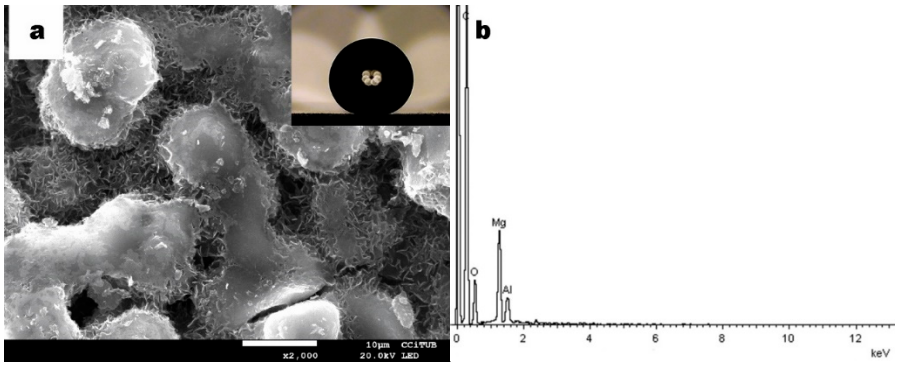

Figure 13. FE-SEM micrograph and EDS spectra shows (**a**) the coating after 10 cycles of abrasive paper test with a smooth structure and (**b**) similar elemental composition after the test is compared to Figure 1c.

One of the most problematic consequences of wear in superhydrophobic surfaces is the loss of character hence moving to hydrophilic surface due to the generation of pinning sites through the whole surface. In fact, due to the homogeneity of flower-like structures of these samples, which are made of the hydrophobic compound magnesium laurate, wear will not introduce hydrophilic character to the as-prepared coating [55–57]. Moreover, as the hierarchical structure is not completely damaged and still present on the surface, and the WCA and the superhydrophobic behavior of the surface is not severely affected. Indeed, the combination of both characteristics, chemical composition homogeneity and hierarchical structure, keeps the Cassie–Baxter wetting state of the coating that promotes superhydrophobicity to the surface. Furthermore, roughness loss does not severely affect its wettability properties, which leads to a durable superhydrophobic surface that also presents self-cleaning properties.

3.4. Water-Harvesting

To understand the capability of the superhydrophobic coating to collect water droplets from the fog/mist environment, the experimental set-up is carried out in a conventional fog chamber. Water collection rate (ξ) was calculated following Equation (1) at different times ranging from 10 min to 120 min:

$$\xi = m_{H2O}/S{\cdot}\mathrm{t} \quad (1)$$

where m is the water mass measured when it is collected, S is the total surface of the coating on to aluminum substrate, and t is time. Samples are placed vertically (90°) and with a tilt (45°) to study the influence of the position in water-harvesting. Figure 14 depicts collecting water rate of coated samples (45° and 90°) and two aluminum substrates as references in both positions (tilt 45° and vertical 90°). As shown, both aluminum references present a water collection rate near zero after 120 min of exposure (6.3×10^{-5} $\mu g{\cdot}mm^{-2}{\cdot}min^{-1}$ in case of 90°, and 3.7×10^{-5} $\mu g{\cdot}mm^{-2}{\cdot}min^{-1}$ for sample tilted 45°), it indicates that these samples are not capable of collection water due to the hydrophilic character of aluminum substrate (WCA = 83 ± 0.9°). Thus, water droplets are strongly adhered on the substrate and cannot slide through the surface to be collected. In the case of coated samples, collection rate increases in both positions but the sample in the vertical position is more efficient; indeed, after 2 h of water collection, the 45° tilt sample allows collection of 9 $\mu g{\cdot}mm^{-2}{\cdot}min^{-1}$ while the vertical sample collects 13 $\mu g{\cdot}mm^{-2}{\cdot}min^{-1}$. Furthermore, in the case of the tilt sample, two different stages of water collection can be identified: the first one from the beginning until it reaches a maximum at 30 min and then remains flat until 60 min of fog test; here, it can be seen that 45° collection rate is higher than the rate of 90° sample (before 40 min); this difference is because at 45° water droplets are slightly retained, which tends to increase their volume and increase the amount of collected water. After this, the second stage behaves in a similar way: water collection rate increases until 90 min and then remains constant until

120 min of fog exposure. This specific behavior is caused by the tilt angle: initially water is collected at a proportional rate for the first 30 min. After that, collection rate remains constant, which indicates a decrease of water collected mass until 60 min of fog exposure. Then, this behavior is repeated with an increase of collected water. In contrast, for the vertically aligned sample, in the first minutes under fog conditions, less quantity of water than in case of tilted sample is collected. Regardless of this difference, collection rate of a vertical sample exceeds the tilted one after 40 min, which indicates that the mass of collected water has increased. Moreover, it can be seen that the amount of collected water increases linearly and constantly during all the experiment.

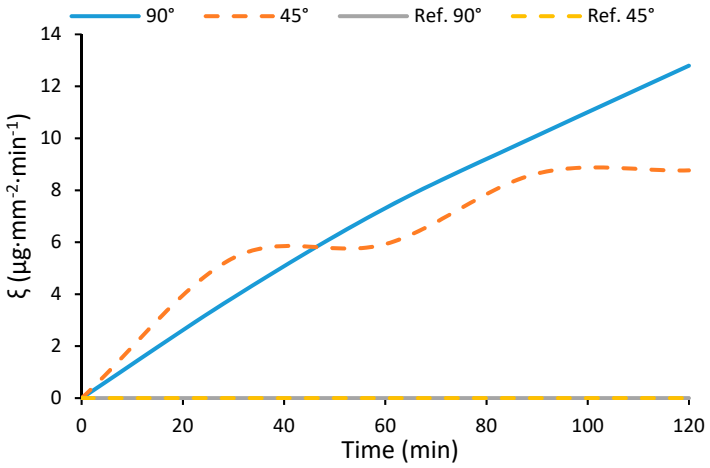

Figure 14. The water collection rate increase in both sample positions, vertically (90°) and tilted (45°) (solid and dotted line, respectively), but it is more pronounced at 90°. References of aluminum substrates (Ref 90° and Ref 45°) are not capable of water collection and are overlapped with x-axis.

Figure 15 depicts coated samples at the beginning of experiment and water droplet condensation after 30 min and 45 min of fog exposure and at the two different tilt angles (90° images at the top row and 45° images at the bottom raw). At 30 min of exposure, water droplets tend to adhere onto the superhydrophobic surfaces and reach an average size of 160 ± 40 μm for both tilt samples. At 45 min of water-harvesting, the size of water droplets at the sample tilted vertically is 286 ± 60 μm and that for 45° is 300 ± 80 μm. Water droplets of the vertically aligned sample (90°) coalesce first, then they increase their size until their diameter (286 ± 60 μm) is exceeded and when they achieve the critical diameter (3.0 ± 0.5 mm), they roll down the surface. Consequently, water droplets leave the surface by gravity and they do it continuously.

As seen in Figure 15, water droplets are adhered to coated surfaces in the initial steps of water collection. It is important to take into account that under fog conditions, water droplet velocity that is increased by the pressure of airstream of fog producer causes them to flatten due to the impact presenting a morphology that can be described as a spherical cap [58]. In fact, water droplets are adhered in planar surfaces until they reach a size of 2.7 mm (according to our result of 3.0 ± 0.5 mm); at this point, by coalescence, the droplets roll off due to the gravity force along the surface [15,59]. In contrast, as the water droplets increase their size, they tend to evaporate, and the water-harvesting efficiency of surfaces significantly decreases. In this experiment, it was found that water droplet diameter at sample tilt 90° is 89% less than that of the maximum size previously mentioned. Thus, this lower size prevents evaporation of water droplets formed onto the coated surface during the water-harvesting process.

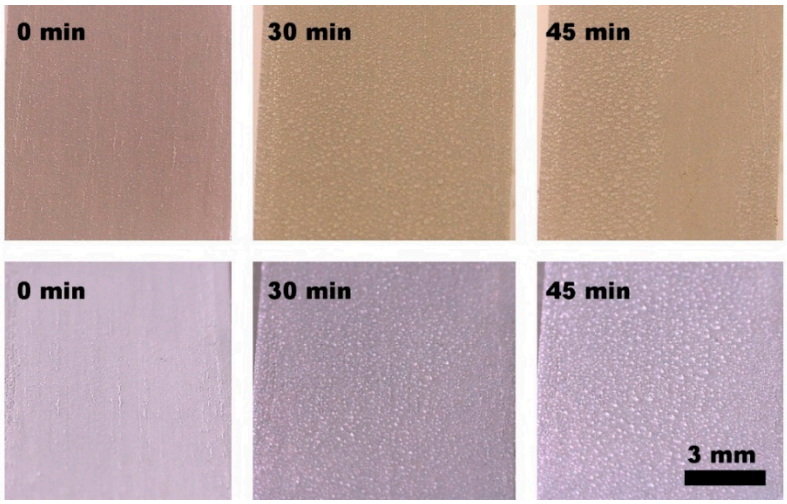

Figure 15. Condensation of water droplets on to superhydrophobic coating. The top images correspond to a tilt of 90° while the bottom images are from the sample tilt 45°. All the images have the same magnification.

Having shown the capability of water-harvesting from fog in the case of superhydrophobic surface tilt 90°, its behavior is discussed considering the surface morphology as well as the hierarchical structure of the as-prepared surface. As described previously, the surface is formed by vertically aligned microarrays with a non-linear cone shape that are combined with flower-like structures leading to a hierarchical structure through the whole surface. Water droplet dynamics is governed by Laplace pressure [60]. In a non-linear cone shape, average Laplace pressure will decrease inside the water droplet, which leads to increase its pressure gradient from the tip to the base of the non-linear cone and the water droplet will move away from the tip on a conical surface [61–63]. Then, the gravitational effect increases and improves water collection from fog.

Apart from the key role of microarrays, it is necessary to consider water-harvesting from the hierarchical structure point of view. On one hand, the flower-like structure, i.e., the micro-scale contribution to the system, presents a diameter of 17.5 ± 3.4 μm. On the other hand, the closed packed nanoarrays from the flower-like structure have a thickness of 32.8 ± 2.9 nm. Actually, flower-like structure morphology behaves as a bump feature that maximizes the vapor-phase diffusion on the apex and water droplet condensation increases onto the surface [15,64]. Simultaneously, the close packed nanoarrays of the structure enable the rapid roll-off of the condensed water droplets from the surface [15].

At this point, when water droplets from fog impact the superhydrophobic surface during the first stages they are adhered since the impact of fog fill the air pockets of the surface. Hence, the Wenzel state responsible for water droplet adhesion is created. Despite that fact, as the impact of fog is continuous, water droplets continuously increase the volume enhanced by coalescence of neighboring droplets until a critical diameter is exceeded. Here, as the cap of water droplets is continuously growing because of fog, their morphology changes to a quasi-spherical morphology. This is caused by low adhesive energy of superhydrophobic surface combined with high surface roughness that results in water droplets being easily detached and rolled off. Thus, this behavior leads to a different wetting state assigned to the Cassie regime. This transition from Wenzel state to Cassie state is governed by roughness and the energy of the system related to the position of liquid–vapor interface [65]. Indeed, the more roughness the surface and higher contact angle, the more possible is this transition between both stable states, and because of higher roughness, Cassie state is more favorable in energetic terms. Additionally, the relationship between transition energy and the height of the liquid–vapor interface depends on the nanostructure and the micro-scale features where the latter gives rise to Wenzel–Cassie transition and the former allows the opposite transition. Here, it is shown that water droplets easily

detach from the superhydrophobic surface and cause the Wenzel–Cassie transition, which indicates that micro-scale features define this phenomenon, leading to an attractive Cassie state that promotes water repellency and improves water droplet detachment and consequently their roll-off.

4. Conclusions

Herein, we present an innovative sustainable surface prepared onto UNS A91070 aluminum substrate showing WCA = 155°, SA = 5° and a CAH = 1°, which makes it suitable as superhydrophobic surface. Based on magnesium laurate ($Mg(C_{11}H_{20}COO)_2$) this compound contributes to decreasing the surface tension of the surface and together with its lamellar structure, traps the air in the pockets through the whole surface. Moreover, the as-prepared surface is highly robust under SiC abrasive paper test where WCA is kept higher than 150° after every abrasive cycle because of its bulk homogeneity composition, showing self-cleaning properties, as well. In addition, its resistance against UV light is shown, retaining its superhydrophobic properties after 300 min of exposure. The combination of the vertically aligned microarrays in a non-linear cone shape and the intrinsic hierarchical structure of the superhydrophobic surface makes it a very convenient system for water collection in a vertical sample position. This innovative superhydrophobic surface opens a new scope with great potential for water-harvesting based on sustainable reactants that provide a focus on solving worldwide problems of human water consumption.

Author Contributions: Conceptualization, O.R.-A. and N.L.-I.; O.R.-A.; investigation, S.F.-P. and O.R.-A.; data curation, S.F.-P. and O.R.-A.; writing—original draft preparation, O.R.-A., S.F.-P. and N.L.-I.; writing—review and editing, O.R.-A. and N.L.-I.; supervision, O.R.-A. and N.L.-I.; All authors have read and agreed to the published version of the manuscript.

Funding: This research received no external funding.

Acknowledgments: The authors would like to acknowledge the support given by Centres Científics i Tecnològics de la Universitat de Barcelona (CCiTUB).

Conflicts of Interest: The authors declare no conflict of interest.

References

1. Bhushan, B.; Jung, Y.C. Natural and biomimetic artificial surfaces for superhydrophobicity, self-cleaning, low adhesion, and drag reduction. *Prog. Mater. Sci.* **2011**, *56*, 1–108. [CrossRef]
2. Gao, L.; McCarthy, T.J. Contact Angle Hysteresis Explained. *Langmuir* **2006**, *22*, 6234–6237. [CrossRef] [PubMed]
3. Nosonovsky, M.; Bhushan, B. Superhydrophobic surfaces and emerging applications: Non-adhesion, energy, green engineering. *Curr. Opin. Colloid Interface Sci.* **2009**, *14*, 270–280. [CrossRef]
4. Liu, M.; Wang, S.; Jiang, L. Nature-inspired superwettability systems. *Nat. Rev. Mater.* **2017**, *2*, 17036. [CrossRef]
5. Su, B.; Tian, Y.; Jiang, L. Bioinspired Interfaces with Superwettability: From Materials to Chemistry. *J. Am. Chem. Soc.* **2016**, *138*, 1727–1748. [CrossRef]
6. Guix, M.; Orozco, J.; Garcia, M.; Gao, W.; Sattayasamitsathit, S.; Merkoçi, A.; Escarpa, A.; Wang, J. Superhydrophobic Alkanethiol-Coated Microsubmarines for Effective Removal of Oil. *ACS Nano* **2012**, *6*, 4445–4451. [CrossRef] [PubMed]
7. Das, A.; Parbat, D.; Shome, A.; Manna, U. Sustainable Biomimicked Oil/Water Wettability That Performs Under Severe Challenges. *ACS Sustain. Chem. Eng.* **2019**, *7*, 11350–11359. [CrossRef]
8. Mobarakeh, L.F.; Jafari, R.; Farzaneh, M. Robust icephobic, and anticorrosive plasma polymer coating. *Cold Reg. Sci. Technol.* **2018**, *151*, 89–93. [CrossRef]
9. Vazirinasab, E.; Jafari, R.; Momen, G. Application of superhydrophobic coatings as a corrosion barrier: A review. *Surf. Coat. Technol.* **2018**, *341*, 40–56. [CrossRef]
10. Zhuo, Y.; Li, T.; Wang, F.; Håkonsen, V.; Xiao, S.; He, J.; Zhang, Z. An ultra-durable icephobic coating by a molecular pulley. *Soft Matter* **2019**, *15*, 3607–3611. [CrossRef]

11. Brassard, J.-D.; Laforte, J.-L.; Blackburn, C.; Perron, J.; Sarkar, D.K. Silicone based superhydrophobic coating efficient to reduce ice adhesion and accumulation on aluminum under offshore arctic conditions. *Ocean Eng.* **2017**, *144*, 135–141. [CrossRef]
12. Masood, M.T.; Zahid, M.; Goldoni, L.; Ceseracciu, L.; Athanassiou, A.; Bayer, I.S. Highly Transparent Polyethylcyanoacrylates from Approved Eco-Friendly Fragrance Materials Demonstrating Excellent Fog-Harvesting and Anti-Wear Properties. *ACS Appl. Mater. Interfaces* **2018**, *10*, 34573–34584. [CrossRef] [PubMed]
13. Dai, X.; Sun, N.; Nielsen, S.O.; Stogin, B.B.; Wang, J.; Yang, S.; Wong, T.-S. Hydrophilic directional slippery rough surfaces for water harvesting. *Sci. Adv.* **2018**, *4*, eaaq0919. [CrossRef]
14. Suvindran, N.; Li, F.; Pan, Y.; Zhao, X. Characterization and Bioreplication of Tradescantia pallida Inspired Biomimetic Superwettability for Dual Way Patterned Water Harvesting. *Adv. Mater. Interfaces* **2018**, *5*, 1–10. [CrossRef]
15. Raut, H.; Ranganath, A.; Baji, A.; Wood, K.L. Bio-inspired hierarchical topography for texture driven fog harvesting. *Appl. Surf. Sci.* **2019**, *465*, 362–368. [CrossRef]
16. Anastas, P.T.; Werner, J. *Green Chemistry: Theory and Practice*; OUP: Oxford, UK, 1998.
17. Erythropel, H.C.C.; Zimmerman, J.B.; De Winter, T.M.; Petitjean, L.; Melnikov, F.; Lam, C.H.; Lounsbury, A.W.; Mellor, K.; Janković, N.Z.; Tu, Q.; et al. The Green ChemisTREE: 20 years after taking root with the 12 principles. *Green Chem.* **2018**, *20*, 1929–1961. [CrossRef]
18. Clark, J.H.; Farmer, T.; Herrero-Davila, L.; Sherwood, J. Circular economy design considerations for research and process development in the chemical sciences. *Green Chem.* **2016**, *18*, 3914–3934. [CrossRef]
19. Klemm, D.; Heublein, B.; Bohn, A.; Fink, H.-P. Cellulose: Fascinating Biopolymer and Sustainable Raw Material. *Angew. Chem. Int. Ed.* **2005**, *44*, 3358–3393. [CrossRef]
20. Calvo-Flores, F.G.; Monteagudo-Arrebola, M.J.; Dobado, J.A.; Isac-García, J. Green and Bio-Based Solvents. *Top. Curr. Chem.* **2018**, *376*, 18. [CrossRef]
21. Spiridon, I.; Darie-Nita, R.N.; Bele, A. New opportunities to valorize biomass wastes into green materials. II. Behaviour to accelerated weathering. *J. Clean. Prod.* **2018**, *172*, 2567–2575. [CrossRef]
22. Zanoletti, A.; Bilo, F.; Depero, L.; Zappa, D.; Bontempi, E. The first sustainable material designed for air particulate matter capture: An introduction to Azure Chemistry. *J. Environ. Manag.* **2018**, *218*, 355–362. [CrossRef] [PubMed]
23. Dichiarante, V.; Milani, R.; Metrangolo, P. Natural surfactants towards a more sustainable fluorine chemistry. *Green Chem.* **2018**, *20*, 13–27. [CrossRef]
24. Schlaich, C.; Yu, L.; Haag, R.; Camacho, L.C.; Wei, Q. Fluorine-free superwetting systems: Construction of environmentally friendly superhydrophilic, superhydrophobic, and slippery surfaces on various substrates. *Polym. Chem.* **2016**, *7*, 7446–7454. [CrossRef]
25. Escobar, A.M.; Llorca-Isern, N. Superhydrophobic coating deposited directly on aluminum. *Appl. Surf. Sci.* **2014**, *305*, 774–782. [CrossRef]
26. Moosavi, S.S.; Norouzbeigi, R.; Velayi, E. Fabrication of flower-like micro/nano dual scale structured copper oxide surfaces: Optimization of self-cleaning properties via Taguchi design. *Appl. Surf. Sci.* **2017**, *422*, 787–797. [CrossRef]
27. Razavi, S.M.R.; Oh, J.; Sett, S.; Feng, L.; Yan, X.; Hoque, M.J.; Liu, A.; Haasch, R.; Masoomi, M.; Bagheri, R.; et al. Superhydrophobic Surfaces Made from Naturally Derived Hydrophobic Materials. *ACS Sustain. Chem. Eng.* **2017**, *5*, 11362–11370. [CrossRef]
28. Selim, M.S.; Elmarakbi, A.; Azzam, A.M.; Shenashen, M.A.; El-Saeed, A.M.; El-Safty, S.A. Eco-friendly design of superhydrophobic nano-magnetite/silicone composites for marine foul-release paints. *Prog. Org. Coat.* **2018**, *116*, 21–34. [CrossRef]
29. Davis, A.; Surdo, S.; Caputo, G.; Bayer, I.S.; Athanassiou, A. Environmentally Benign Production of Stretchable and Robust Superhydrophobic Silicone Monoliths. *ACS Appl. Mater. Interfaces* **2018**, *10*, 2907–2917. [CrossRef]
30. Yue, X.; Zhang, T.; Yang, D.; Qiu, F.; Li, Z. Hybrid aerogels derived from banana peel and waste paper for efficient oil absorption and emulsion separation. *J. Clean. Prod.* **2018**, *199*, 411–419. [CrossRef]
31. Moreno, E.; Cordobilla, R.; Calvet, T.; Cuevas-Diarte, M.A.; Gbabode, G.; Negrier, P.; Mondieig, D.; Oonk, H.A.J. Polymorphism of even saturated carboxylic acids from n-decanoic to n-eicosanoic acid. *New J. Chem.* **2007**, *31*, 947. [CrossRef]

32. Nelson, P.N.; Taylor, R.A. Powder X-ray diffraction, infrared and 13C NMR spectroscopic studies of the homologous series of some solid-state zinc(II) and sodium(I) n-alkanoates. *Spectrochim. Acta Part A: Mol. Biomol. Spectrosc.* **2015**, *138*, 800–806. [CrossRef]
33. Hartman, P. Structural morphology of organic compounds having two centrosymmetric molecules in a monoclinic unit cell. *J. Cryst. Growth* **1991**, *110*, 559–570. [CrossRef]
34. Bond, A.D. On the crystal structures and melting point alternation of the n-alkyl carboxylic acids. *New J. Chem.* **2004**, *28*, 104–114. [CrossRef]
35. Cassie, A.B.D.; Baxter, S. Wettability of porous surfaces. *Trans. Faraday Soc.* **1944**, *40*, 546. [CrossRef]
36. Gadermann, M.; Preston, T.C.; Troster, C.; Signorell, R. Characterization of palmitic and lauric acid aerosols from rapid expansion of supercritical CO_2 solutions. *Mol. Phys.* **2008**, *106*, 945–953. [CrossRef]
37. Caroline, M.L.; Vasudevan, S. Growth and characterization of an organic nonlinear optical material: L-alanine alaninium nitrate. *Mater. Lett.* **2008**, *62*, 2245–2248. [CrossRef]
38. Jiesheng, L.; Yuanyuan, Y.; Xiang, H. Research on the preparation and properties of lauric acid/expanded perlite phase change materials. *Energy Build.* **2016**, *110*, 108–111. [CrossRef]
39. Yin, W.Z.; Tan, Q.; Liu, L.; Li, X.L. Synthesis and Characterization of Mg-Al Layered Double Hydroxide. *Adv. Mater. Res.* **2012**, *454*, 101–104. [CrossRef]
40. Dang, L.; Nai, X.; Zhu, D.; Jing, Y.; Liu, X.; Dong, Y.; Li, W. Study on the mechanism of surface modification of magnesium oxysulfate whisker. *Appl. Surf. Sci.* **2014**, *317*, 325–331. [CrossRef]
41. Robinet, L.; Corbeil-A2, M.-C. The Characterization of Metal Soaps. *Stud. Conserv.* **2003**, *48*, 23–40. [CrossRef]
42. Otero, V.; Sanches, D.; Montagner, C.; Vilarigues, M.; Carlyle, L.; Lopes, J.; Melo, M.J. Characterisation of metal carboxylates by Raman and infrared spectroscopy in works of art. *J. Raman Spectrosc.* **2014**, *45*, 1197–1206. [CrossRef]
43. Saggu, M.; Liu, J.; Patel, A.R. Identification of Subvisible Particles in Biopharmaceutical Formulations Using Raman Spectroscopy Provides Insight into Polysorbate 20 Degradation Pathway. *Pharm. Res.* **2015**, *32*, 2877–2888. [CrossRef]
44. De Gelder, J.; De Gussem, K.; Vandenabeele, P.; Moens, L. Reference database of Raman spectra of biological molecules. *J. Raman Spectrosc.* **2007**, *38*, 1133–1147. [CrossRef]
45. Czamara, K.; Majzner, K.; Pacia, M.; Kochan, K.; Kaczor, A.; Baranska, M. Raman spectroscopy of lipids: A review. *J. Raman Spectrosc.* **2014**, *46*, 4–20. [CrossRef]
46. De Veij, M.; Vandenabeele, P.; De Beer, T.; Remon, J.P.; Moens, L. Reference database of Raman spectra of pharmaceutical excipients. *J. Raman Spectrosc.* **2009**, *40*, 297–307. [CrossRef]
47. Men, S.; Jiang, X.; Xiang, X.; Sun, G.; Yan, Y.; Lyu, Z.; Jin, Y. Synthesis of Cellulose Long-Chain Esters in 1-Butyl-3-methylimidazolium Acetate: Structure-Property Relations. *Polym. Sci. Ser. B* **2018**, *60*, 349–353. [CrossRef]
48. Cocco, F.; Elsener, B.; Fantauzzi, M.; Atzei, D.; Rossi, A. Nanosized surface films on brass alloys by XPS and XAES. *RSC Adv.* **2016**, *6*, 31277–31289. [CrossRef]
49. Wu, P.-Y.; Jiang, Y.-P.; Zhang, Q.-Y.; Jia, Y.; Peng, D.-Y.; Xu, W. Comparative study on arsenate removal mechanism of MgO and MgO/TiO2 composites: FTIR and XPS analysis. *New J. Chem.* **2016**, *40*, 2878–2885. [CrossRef]
50. Dobrovolsky, V.; Khyzhun, O.; Sinelnichenko, A.; Ershova, O.; Solonin, Y. XPS study of influence of exposure to air on thermal stability and kinetics of hydrogen decomposition of MgH 2 films obtained by direct hydrogenation from gaseous phase of metallic Mg. *J. Electron Spectrosc. Relat. Phenom.* **2017**, *215*, 28–35. [CrossRef]
51. Zhang, B.; Li, Y.; Hou, B. One-step electrodeposition fabrication of a superhydrophobic surface on an aluminum substrate with enhanced self-cleaning and anticorrosion properties. *RSC Adv.* **2015**, *5*, 100000–100010. [CrossRef]
52. Chen, L.; Meng, H.; Jiang, L.; Wang, S. Fatty-Acid-Metal-Ion Complexes as Multicolor Superhydrophobic Coating Materials. *Chem.–Asian J.* **2011**, *6*, 1757–1760. [CrossRef] [PubMed]
53. Wang, Z.; Elimelech, M.; Lin, S. Environmental Applications of Interfacial Materials with Special Wettability. *Environ. Sci. Technol.* **2016**, *50*, 2132–2150. [CrossRef] [PubMed]
54. Xiong, J.; Sarkar, D.K.; Chen, X.G. Ultraviolet-Durable Superhydrophobic Nanocomposite Thin Films Based on Cobalt Stearate-Coated TiO2 Nanoparticles Combined with Polymethylhydrosiloxane. *ACS Omega* **2017**, *2*, 8198–8204. [CrossRef]

55. Verho, T.; Bower, C.; Andrew, P.; Franssila, S.; Ikkala, O.; Ras, R.H.A. Mechanically Durable Superhydrophobic Surfaces. *Adv. Mater.* **2010**, *23*, 673–678. [CrossRef]
56. Milionis, A.; Loth, E.; Bayer, I.S. Recent advances in the mechanical durability of superhydrophobic materials. *Adv. Colloid Interface Sci.* **2016**, *229*, 57–79. [CrossRef] [PubMed]
57. Mortazavi, V.; Khonsari, M. On the degradation of superhydrophobic surfaces: A review. *Wear* **2017**, *372*, 145–157. [CrossRef]
58. Welsh, A.; Hou, M.; Meriki, N.; Stevenson, G. Use of Four-Dimensional Analysis of Power Doppler Perfusion Indices to Demonstrate Cardiac Cycle Pulsatility in Fetoplacental Flow. *Ultrasound Med. Boil.* **2012**, *38*, 1345–1351. [CrossRef]
59. De Gennes, P.-G.; Brochard-Wyart, F.; Quéré, D. *Capillarity and Wetting Phenomena*, 1st ed.; Springer: Berlin/Heidelberg, Germany, 2004.
60. Guan, Y.; Cheng, F.; Pan, Z. Superwetting polymeric three dimensional (3D) porous materials for Oil/Water separation: A Review. *Coatings* **2019**, *11*, 806. [CrossRef]
61. Lin, J.; Tan, X.; Shi, T.; Tang, Z.; Liao, G. Leaf Vein-Inspired Hierarchical Wedge-Shaped Tracks on Flexible Substrate for Enhanced Directional Water Collection. *ACS Appl. Mater. Interfaces* **2018**, *10*, 44815–44824. [CrossRef]
62. Zhang, S.; Huang, J.; Chen, Z.; Lai, Y. Bioinspired Special Wettability Surfaces: From Fundamental Research to Water Harvesting Applications. *Small* **2016**, *13*, 1602992. [CrossRef]
63. Gurera, D.; Bhushan, B. Bioinspired conical design for efficient water collection from fog. *Philos. Trans. R. Soc. A Math. Phys. Eng. Sci.* **2019**, *377*, 20190125. [CrossRef] [PubMed]
64. Park, K.-C.; Kim, P.; Grinthal, A.; He, N.; Fox, D.; Weaver, J.C.; Aizenberg, J. Condensation on slippery asymmetric bumps. *Nature* **2016**, *531*, 78–82. [CrossRef] [PubMed]
65. Nosonovsky, M.; Bhushan, B. Patterned Nonadhesive Surfaces: Superhydrophobicity and Wetting Regime Transitions. *Langmuir* **2008**, *24*, 1525–1533. [CrossRef] [PubMed]